International Forum on Aeroelasticity and Structural Dynamics
IFASD 2024
17-21 June 2024, The Hague, The Netherlands

EXPERIMENTAL AND NUMERICAL ACTIVITIES FOR AEROELASTIC ANALYSIS OF AN ALUMINUM WING

Davide Mastrodicasa[1], Silvia Vettori[1], Massimiliano Chillemi[1,2], Aleli Sosa Chavez[1,3], Alessandro Laurini[1,3], Emilio Di Lorenzo[1], and Karl Janssens[1]

[1] Siemens Digital Industries Software, Interleuvenlaan 68, 3001 Leuven, Belgium
[2] University of Messina, Contrada Di Dio, 98166 Sant'Agata, Messina, Italia
[3]University of Rome La Sapienza, Via Eudossiana, 18, 00184 Roma, Italia

Keywords: FSI, Kalman Filter, Digital Image Correlation, CFD

Abstract: In the aerospace field, comprehensive monitoring of systems structural behavior is imperative for enhancing structural safety, optimizing maintenance protocols, and predicting remaining useful life. New significant challenges have been raised in recent years by market innovations such as the use of composite materials and high aspect ratio geometries. These solutions generate lightweight components featuring larger deformations with increasing fluid loading. To deal with these features, this work pursues the long-term goal of establishing a validated procedure that combines the use of different methodologies for Fluid-Structure Interaction (FSI) problems. A multi-physics environment, including experimental and numerical analyses, is constructed to allow for FSI analysis of an aluminum wing featuring a NACA 0018 profile during wind tunnel testing.

An extensive test campaign has been conducted on such specimen in the wind tunnel of the University of Twente adopting a clamped-free configuration. The unit under test has been instrumented with different measurement systems such as strain gauges, pressure ports, and high-speed cameras for vision-based methods.

To complement the experimental activities, both a structural and an aerodynamic model have been built and validated using experimental reference data. The Finite Element Model (FEM) has been built in Simcenter 3D and updated to match the experimental modal parameters identified via Experimental Modal Analysis (EMA) during an impact test conducted prior to wind tunnel testing. A Computational Fluid Dynamics (CFD) analysis has been conducted in Simcenter STAR CCM+ and validated via experimental pressure values.

To pursue the objective of implementing a comprehensive FSI framework for aeroelastic analysis, a first step proposed in this work consists in combining the validated FEM with a few strain measurements to reconstruct the full-field structural response as well as the pressure field around the wing during testing. This approach, referred to as Virtual Sensing (VS) is hereby implemented using a modified version of the Augmented Kalman Filter (AKF), tailored for applications involving distributed loading conditions. The achieved results are validated against the full-field measurements extracted via DIC.

1 INTRODUCTION

In the aerospace industry, ensuring the structural integrity and performance of aircraft components is paramount for maintaining safety standards, optimizing maintenance schedules, and prolonging the lifespan of these systems. The ongoing evolution of aerospace technology, marked by the introduction of composite materials and high aspect ratio geometries, has significantly influenced the structural characteristics of modern aircraft. These innovations, while providing benefits such as reduced weight and improved aerodynamic efficiency, introduce new complexities in the behavior of these components under operational conditions. Notably, lightweight structures are prone to larger deformations and are more sensitive to fluid dynamic loads, necessitating advanced methodologies for comprehensive structural monitoring and analysis [1]. Fluid-Structure Interaction (FSI) represents a critical area of study within this context. FSI refers to the coupling between fluid flow and structural response, where the movement of the fluid affects the structure and vice versa. Understanding FSI is crucial for predicting the performance and potential failure modes of aerospace structures under various loading conditions [2].

During the past years, FSI studies have mainly focused on coupling structural numerical modeling and fluid loading using Finite Element Analysis (FEA) and Computational Fluid Dynamics (CFD) respectively [3] [4]. Many methods are available in isolation for validating FEA and CFD. However, there is a lack of experimental validation data for FSI investigations associated with accurate measurement of structural deformation under fluid loading.

One of the challenges related to experimentally measuring the structural dynamic behavior of a structure subjected to wind excitation is related to instrumenting the structure under test. Placing sensor such as strain gauges and accelerometers have a huge impact on the tested structure both on mass distribution and airflow interaction. Vision-based methods such as Digital Image Correlation (DIC) can overcome this challenge due to their contactless nature. The response of solid structures to dynamic fluid loading can be evaluated from direct deformation measurements through the use of high-speed cameras. In addition to providing dynamic displacement information, DIC yields surface strain measurement. Multiple works have been published in this domain. In [5], the feasibility of a combined PIV and DIC system is demonstrated for full-field flow pressure estimation and structural deformation measurement. In addition, an investigation related to the robustness of the pressure reconstruction with respect to image resolution, field of view, and interrogation window size is performed. A similar work has been published in [6] presenting a first application of the combination PIV and DIC in a towing tank environment for the analysis of a flexible hydrofoil.

An alternative approach to DIC for gaining full-field knowledge of the structural behavior of a system from a limited number of sensed locations, comprises the implementation of reliable Kalman-based methodologies, such as the Augmented Kalman Filter (AKF) for combining model-based and data-based information. These approaches, often referred to as Virtual Sensing (VS) methods, can be adopted to infer unmeasured responses and/or unknown loads in dynamic environments by combining a limited set of physical measurements with a structural time-domain model of the tested specimen. This allows for the reduction of the necessary physical sensors, thus limiting their downsides such as mass loading and airflow interaction. In this sense, VS can also be adopted as a complementary solution to DIC for reconstructing realistic structural responses at locations that cannot be framed by cameras, e.g., internal areas of a specimen.

This paper aims to tackle the current challenges in FSI analysis by creating and validating a comprehensive framework that combines experimental and numerical approaches. The use of numerical approaches allows for a deeper understanding of the relationship between aerodynamic loads and structural responses, which in turn improves structural safety and aids in the development of predictive maintenance strategies. By combining experimental data with advanced numerical simulations, this study demonstrates a robust approach to tackling the complexities of FSI in aerospace applications. The focus of this work is on a case study involving wind tunnel testing of an aluminum wing with a NACA 0018 profile. This type of airfoil is widely used in aerodynamic research due to its symmetrical shape and well-documented aerodynamic properties, making it an ideal candidate for FSI studies.

An extensive experimental campaign was conducted in the wind tunnel at the University of Twente, where the wing was tested in a clamped-free configuration. This setup simulates real-world boundary conditions and allows for the assessment of the wing response to various flow velocities and angles of attack (AoA). The wing was instrumented with multiple measurement systems to capture detailed data on its structural and aerodynamic behavior. Strain gauges were used to measure structural deformations, pressure ports provided information on the pressure distribution around the wing, and high-speed cameras combined with DIC were employed to measure full-field displacements on the surface.

Parallel to the experimental efforts, a Finite Element Model (FEM) was developed using Simcenter 3D to numerically simulate the wing dynamic properties. The FEM was validated and updated based on experimental modal parameters obtained from an impact test conducted with the same setup adopted during wind tunnel testing. This step ensures an accurate numerical representation of the wing's physical behavior, thereby enhancing the reliability of subsequent analyses. In addition to the structural analysis, a Computational Fluid Dynamics (CFD) study was performed using Simcenter STAR CCM+. This CFD analysis provided detailed insights into the aerodynamic forces acting on the wing and was validated against the experimental pressure data collected during wind tunnel testing. The validated CFD model, together with the FEM, form the basis for the integrated FSI framework.

2 THEORETICAL BACKGROUND

2.1 Digital Image Correlation (DIC)

Digital Image Correlation (DIC) is a measuring technique that can be used to obtain three-dimensional full field shape, displacement, and strain of a surface, both in static or dynamic conditions, under any arbitrary load. It is an optical-numerical method since on one side optical sensors (such as cameras or microscopes) are used to acquire images of something deforming and in the other side there is a software platform where the images are loaded and processed. DIC works in a pattern tracking base so contrast in the surface is always needed. Natural contrast like the surface texture or the material microstructure can be used but the contrast can also be created with stickers, markers, or spray paint for example. This allows to track the position of the pixels across different pictures, the main goal of the correlation process. While with only one camera the system is limited to measurements in two in-plane directions, with two or more cameras, in what is called a stereo system, there is the possibility of measuring in three directions. Each camera observes the surface of the specimen from a different direction so, performing a triangulation

process, allows to retrieve the coordinates of the points in space. The scheme of the work principle of 3D DIC is in Figure 1.

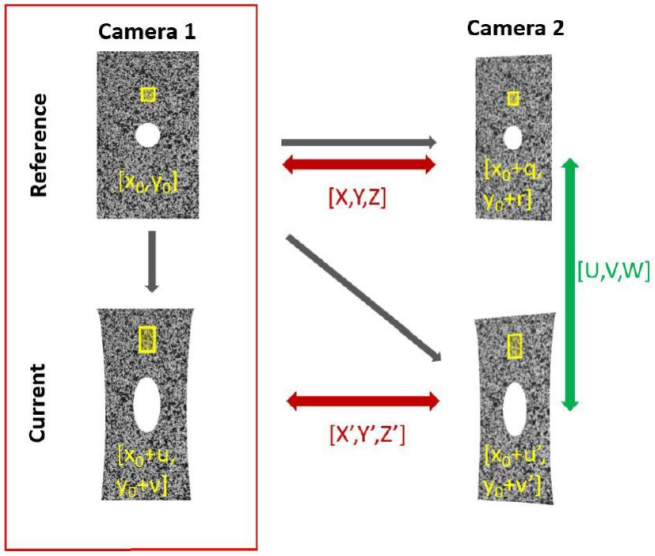

Figure 1: Working principle of stereo DIC.

The first image acquired for camera 1 is used as reference and the first image acquired for camera 2, at the same time, is compared to it. After performing the calibration process, the relative orientation of cameras is known so the corresponding points in the images from the two different cameras can be triangulated to the real position of the point in the space, represented in Figure 1 by [X,Y,Z]. This process is repeated along the time to track the position of each one of the measurement points during the test. Hence, the correlation process retrieves all the deformation of the surface under analysis, denoted as [U,V,W] in the scheme.

2.2 The Augmented Kalman Filter (AKF)

Kalman-based VS strategies can be employed in structural dynamics for reconstructing the full-field responses and unknown loads leveraging the combination of a few measurements a structural model, i.e., a FEM. Among these methods, the AKF stands as a powerful algorithm for joint input-state estimation. This approach relies on the so-called state augmentation, according to which, given a structural state-space model [7], an augmented state vector is constructed by grouping the system state vector and the unknown input vector. In doing so, the unknown input excitation can be treated as an additional variable to be estimated via a Kalman filtering scheme.
The augmented time-discrete form of a state-space model describing the dynamics of a structural system can be constructed as follows starting from the FEM structural matrices:

$$\mathbf{x}_k^{\mathrm{a}} = \mathbf{F}^{\mathrm{a}}\mathbf{x}_{k-1}^{\mathrm{a}} + \mathbf{w}_{k-1}^{\mathrm{a}}$$
$$\mathbf{y}_k = \mathbf{C}^{\mathrm{a}}\mathbf{x}_k^{\mathrm{a}} + \mathbf{v}_k$$

where all the inputs applied to the system are assumed to be unknown and have been embedded in the augmented state vector $\mathbf{x}^{\boldsymbol{a}}$ as follows:

$$\mathbf{x}^{\mathrm{a}} = [\mathbf{x}^T\ \mathbf{u}^T]^T.$$

The state-space matrices are constructed accordingly and mutually uncorrelated Gaussian noises $\mathbf{w}$ and $\mathbf{v}$ have been introduced to respectively consider model uncertainties and measurement noise. Moreover, a zeroth-order random walk model has been adopted to model the unknown input dynamics [7]. The covariance matrices associated to $\mathbf{w}^{\boldsymbol{a}}$ and $\mathbf{v}$ are respectively denoted as $\mathbf{R}$ and $\mathbf{Q}^{\mathrm{a}}$.
The discrete-time formulation of the AKF can be split into two sequential steps as follows:

1. Time Update:

$$\hat{\mathbf{x}}_k^{\mathrm{a}-} = \mathbf{F}^{\mathrm{a}}\,\hat{\mathbf{x}}_{k-1}^{\mathrm{a}+}$$
$$\mathbf{P}_{\mathrm{k}}^{-} = \mathbf{F}^{a}\mathbf{P}_{\mathrm{k}-1}^{+}\,\mathbf{F}^{\mathrm{aT}} + \mathbf{Q}^{a}$$

2. Measurement Update:

$$\mathbf{K}_k = \mathbf{P}_k^{-}\mathbf{C}^{\mathrm{aT}}\,\mathbf{C}^{\mathrm{a}}\boldsymbol{P}_k^{-}\mathbf{C}^{aT} + \boldsymbol{R}^{-1}$$
$$\hat{\mathbf{x}}_k^{\mathrm{a}+} = \hat{\mathbf{x}}_k^{\mathrm{a}-} + \mathbf{K}_k(\mathbf{y}_k - \mathbf{C}^{\mathrm{a}}\,\hat{\mathbf{x}}_k^{\mathrm{a}-})$$
$$\mathbf{P}_k^{+} = (\mathbf{I} - \mathbf{K}_k\mathbf{C}^{a})\mathbf{P}_k^{-}$$

where $\mathbf{P}_k =$ is the error covariance, the trace of which is minimized by the AKF. Once the estimated augmented state vector $\hat{\mathbf{x}}^{\mathrm{a}+}$ has been obtained, it can be used for estimating the unmeasured responses vector writing the state-space output equation for the FEM Degrees of Freedom (DOFs) to be estimated.

3 CASE STUDY: WIND TUNNEL TEST OF A NACA 0018 WING

This Section describes the experimental setup for wind tunnel measurements on a NACA 0018 wing. The modal hammer test results are presented and their used for validation of the FEM is discussed. The validated FE Model is then employed in a AKF scheme, and the estimated inputs and responses are compared with their measured counterparts.

3.1 Experimental Setup

The wind tunnel test presented in this work has been conducted at the University of Twente on an aluminum wing featuring a NACA0018 airfoil. The testing configuration, shown in Figure 2, involved clamping the wing in a clamped-free setup using three mountings. The NACA0018 airfoil is known for its symmetrical shape about the chord line, 0% camber, and a maximum thickness of 18% of the chord length. The wing dimensions include a wingspan of 1200 mm and a chord length of 165 mm. The flow wet area, spanning 700 mm along the wingspan, actively interacts with the airflow during the test. The aluminum construction of the airfoil is favored in aerospace for its exceptional strength-to-weight ratio, corrosion resistance, and ease of machining. During the extensive test campaign, different flow velocities have been adopted in combination with two alternative AoA: 0 and 10 degrees.

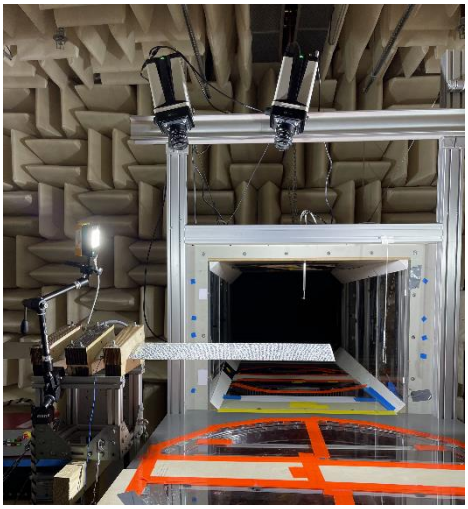

Figure 2: Wind tunnel test setup.

Various sensors were used, including uniaxial strain gauges, rosettes, and pressure ports. A total of 23 deformation measurements (7 uniaxial strain gauges in the z-direction and 7 rosettes in the x and z-directions[1]) and 19 pressure measurements were acquired. These sensors were placed on specific sections along the span, distributed over both the suction and pressure sides. The exact positions of these sensors are shown in Figure 3.

Surface displacement measurements during the wind tunnel test were conducted using vision-based methods such as 3D-DIC. This method involves capturing images of the specimen from different perspectives using two cameras, enabling three-dimensional measurements. Two high-speed cameras iX i-Speed 510 with a resolution of 1920x1080 Px running at 800 Hz were used for the measurement campaign.

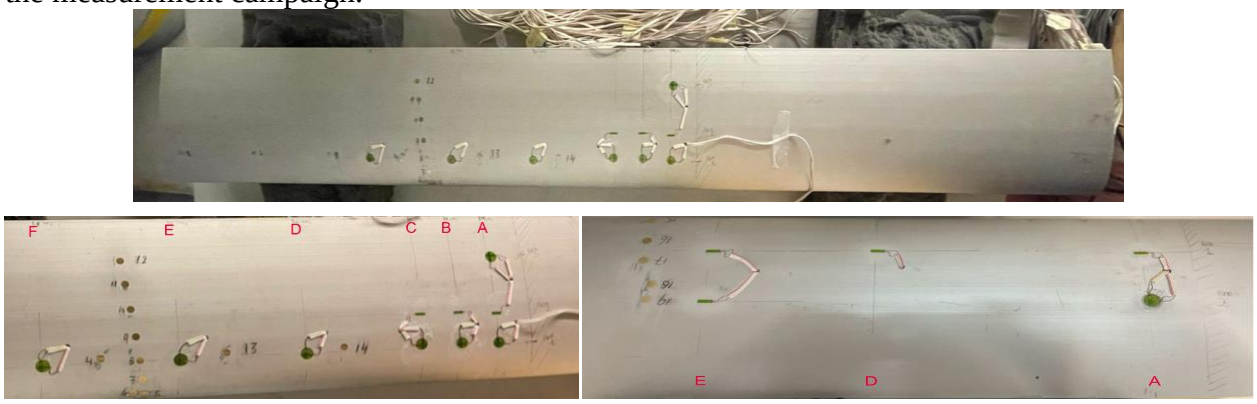

Figure 3: Airfoil instrumentation on the suction side (top and left) and pressure side (right).

The essential steps, from experimental setup preparation to image acquisition, taken during the test campaign are the following:

- Prior to actual testing, a calibration process was carried out to establish the intrinsic and extrinsic of the stereo camera system. The intrinsic parameters allow to estimate the internal parameters of each camera, such as focal length, optical center, and lens distortion. The extrinsic parameters allow to estimate the roto translation matrix between the cameras in the stereo system.

[1] In this case, the z-direction is the span-wise direction. While the x-direction is the chord-wise direction.

- A speckle pattern was applied to the upper surface of the airfoil by using glued paper. This pattern, consisting of randomly distributed dots, serves as a unique identifier for each point on the surface.
- To ensure consistent and uniform lighting conditions, artificial light sources were employed during the measurements. Controlled lighting helps in achieving clear and well-contrasted images, which is essential for accurate DIC measurements.
- The cameras were positioned to capture images of the aluminum airfoil during the aerodynamic excitation.

The experimental setup is illustrated in Figure 4.

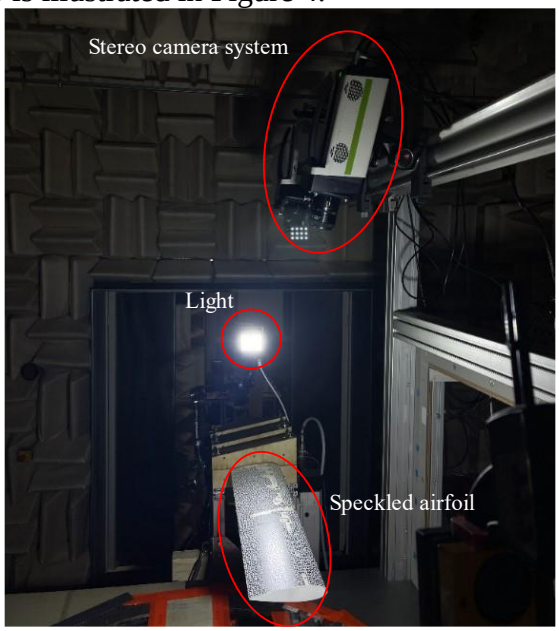

Figure 4: DIC setup during the wind tunnel test.

3.2 Experimental Modal Analysis for Finite Element Analysis Validation

Prior to employment of VS techniques, it is crucial to validate the available FE Model. The accuracy of the simulation model in representing the structure physical behavior is a critical factor in obtaining reliable estimation values via VS. To validate the FE Model, a modal hammer test is performed on the structure for estimation of modal parameters (natural frequency, modal damping) and structural mode shapes. The experimental setup, shown in Figure 5 together with the Simcenter Testlab geometry, includes 10 accelerometers.

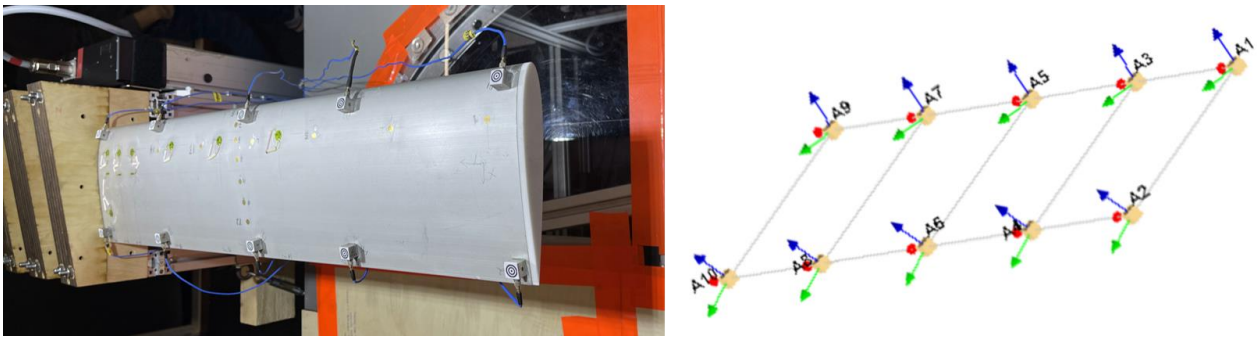

Figure 5: EMA Experimental setup and Simcenter Testlab geometry.

The first 10 modes of the structure were estimated through Simcenter PolyMax. Natural frequencies and modal damping ratios of the selected modes are summarized in Table *1*.

Modes	Natural frequency [Hz]	Damping ratio [%]
1	40.48	1.83
2	158.72	2.04
3	263.45	1.91
4	371.94	2.64
5	623.03	1.61
6	942.47	1.07
7	1016.03	0.73
8	1055.76	0.93
9	1211.34	1.13
10	1329.11	0.63

Table 1: EMA Modal parameters.

A realistic FEM, depicted in Figure 6, was developed in Simcenter 3D relying on the dimensions and weight of the actual wing (made in 6061-T6 aluminum). Realistic Boundary Conditions (BCs), where simulated by including three bands of constrained nodes with 56 mm, 73 mm, and 60 mm length. The displacement in y-direction has been blocked for the nodes within these zones, while still allowing reduced dynamic movement in the other two directions.

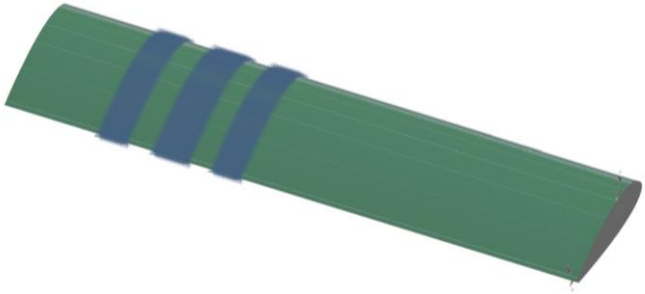

Figure 6: FE Model and BCs.

The first 10 modes of the structure have been computed via NX Nastran SOL103 in Simcenter 3D. Two criteria, namely the frequency errors and Modal Assurance Criterion (MAC), were used to correlate the simulation and experimental modal parameters to ensure that the model faithfully represents the dynamic characteristics of the physical structure:

$$\Delta f_i = \frac{f_{sim_i} - f_{exp_i}}{f_{exp_i}} \cdot 100 \qquad MAC_{i,j} = \frac{\Psi_{exp_i}^T \Psi_{sim_j}}{\sqrt{\Psi_{exp_i}^T \Psi_{exp_i} \Psi_{sim_j}^T \Psi_{sim_j}}}$$

where f_{sim_i} and f_{exp_i} are the undamped natural frequencies of the simulation and test model, respectively. Ψ_{exp_i} and Ψ_{sim_j} are the experimental and simulated mode shapes respectively. The results in terms of MAC and natural frequency error are reported in Figure 7 and

.

Modes	Exp Natural frequency [Hz]	Sim Natural frequency [Hz]	Δf [%]
1	40.48	40.3	-0.47
2	158.72	191.9	20.89
3	263.45	237.1	-10.02
4	371.94	314.8	-15.39
5	623.03	601.4	-3.49
6	942.47	880.9	-6.54
7	1016.03	986.6	-2.90
8	1055.76	989.4	-6.29
9	1211.34	1300	7.39
10	1329.11	1351	1.67

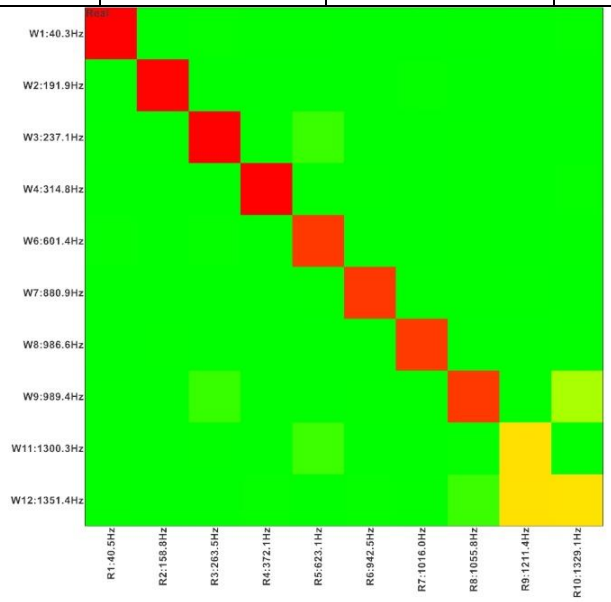

Figure 7: MAC diagram between test and simulation mode shapes.

Modes	Exp Natural frequency [Hz]	Sim Natural frequency [Hz]	Δf [%]
1	40.48	40.3	-0.47
2	158.72	191.9	20.89
3	263.45	237.1	-10.02
4	371.94	314.8	-15.39
5	623.03	601.4	-3.49
6	942.47	880.9	-6.54
7	1016.03	986.6	-2.90
8	1055.76	989.4	-6.29
9	1211.34	1300	7.39
10	1329.11	1351	1.67

Table 2: Natural frequency comparing table between test and simulation.

3.3 Full-field response estimation through VS and DIC

During the wind tunnel test campaign described in Section 3.1, several test runs have been performed adopting different flow velocities and AoA. The test run analyzed in this work featured 50 m/s flow velocity and 10 degrees AoA. The measurements have been initiated at 0 m/s and the flow speed has been increased linearly up to the final value of 50 m/s.

3.3.1 DIC Analysis and Geometry Alignment

The DIC analysis was conducted using the Testlab DIC software. A total of 38438 images, sampled at 800 Hz, were processed. The DIC correlation settings were optimized to provide accurate analysis and valuable insights into displacements, particularly in the out-of-plane direction (w). The qualitative assessment of these displacements showed a strong alignment with the expected behavior. The observed shape of the displacements, as shown in Figure 8, accurately reflects the anticipated pattern, starting from zero and progressively increasing during the initial phase of the test run-up. Then, the displacements reach a steady state value for the remaining duration of the test. This qualitative consistency demonstrates the reliability of the DIC correlation methodology in capturing the dynamic behavior of the specimen and providing a clear representation of the displacements throughout the wind tunnel test.

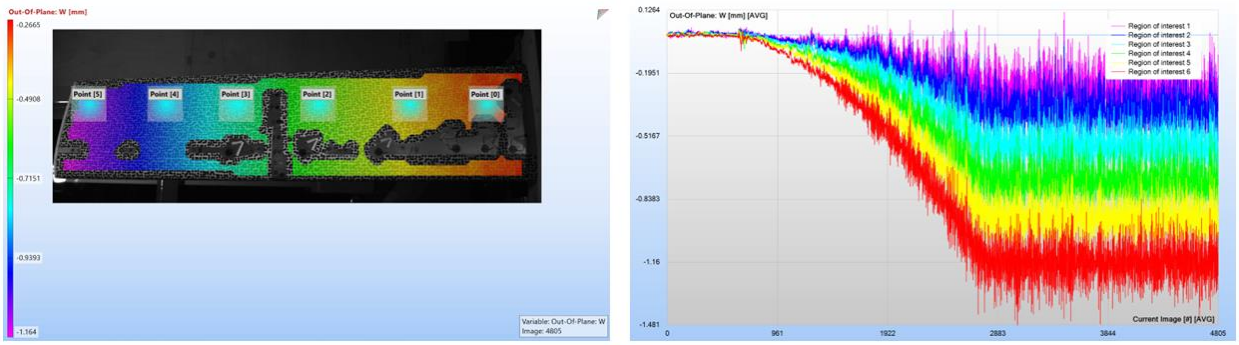

Figure 8: Extraction of six individual points and their displacements.

To facilitate the comparison between structural responses gathered via DIC and VS, the initial step consists in aligning the DIC and FE Model geometries. This involves selecting at least three common points in both DIC and FE geometries to accurately project the FE point cloud onto the DIC reference system. The process includes executing this alignment multiple times by choosing different points. This trial-and-error approach provides flexibility in refining the alignment process, taking into account the user's visual selection of reference points. The details of this process are illustrated in Figure 9.

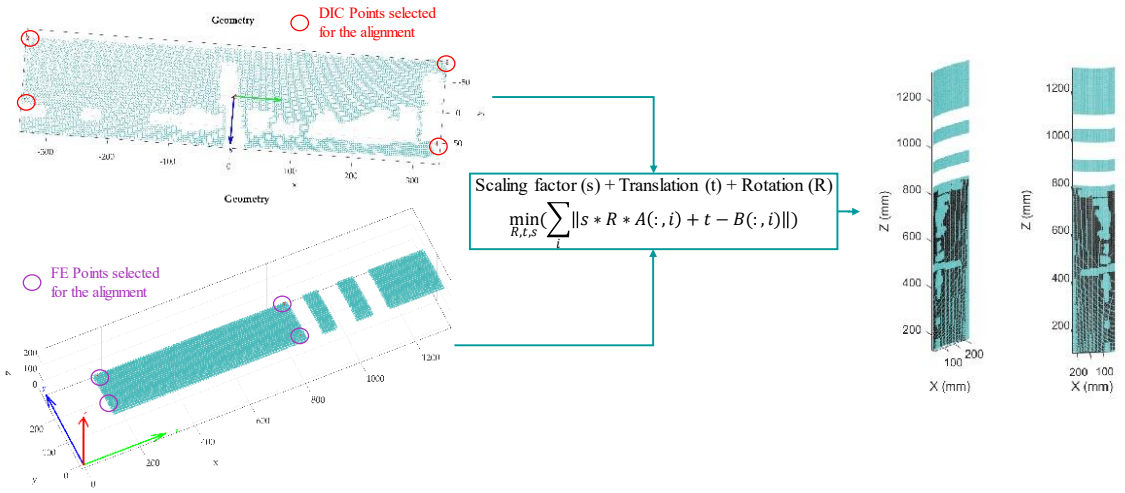

Figure 9: DIC and FE geometry alignment procedure.

An error map, Figure 10, was created to assess the alignment between the two geometries during various trials. The accuracy of the estimation was determined by selecting the trial that minimizes the mean distance between each point cloud of the DIC geometry and its nearest node of the FE mesh.

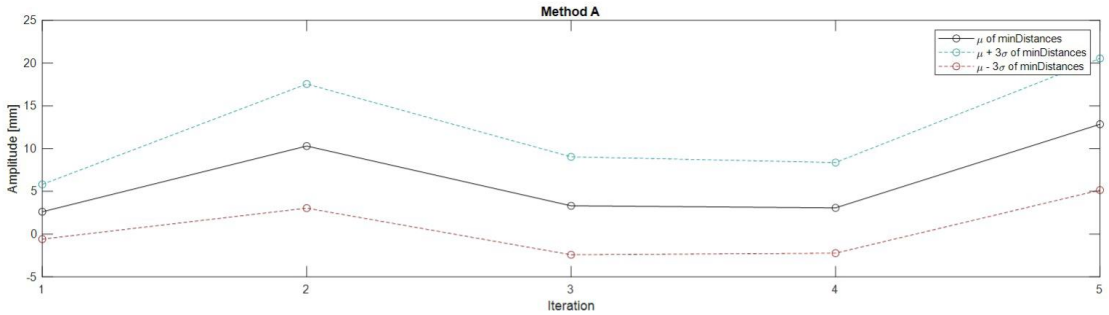

Figure 10: Mean and uncertainty bounds of the minimum distances computed during the geometry alignment trials.

3.3.2 Virtual Sensing for full-field response estimation under distributed loading conditions

An extension of the AKF algorithm reported in Section 2.2 has been constructed for the case study presented in this work in order to account for the distributed nature of the aerodynamic loads. To model the distributed load, a shape matrix $\boldsymbol{\Psi}$ is included in the structural state-space equation to map a few master loads (included in the vector $\tilde{\mathbf{u}}$) over the entire wet area invested by the flow. This assumption turns the time-discrete state equation into:

$$\mathbf{x}_k = \mathbf{F}\,\mathbf{x}_{k-1} + \mathbf{B}\boldsymbol{\Psi}\tilde{\mathbf{u}}_{k-1}.$$

Adopting this modification, the AKF can then be applied using the equations reported in Section 2.2 for simultaneously estimating the master loads vector and the unmeasured responses. The employed shape matrix describes the pressure distribution over the wing wet surface. The experimentally derived distribution of the normalized pressure along the airfoil chord and span, is shown in Figure 11.

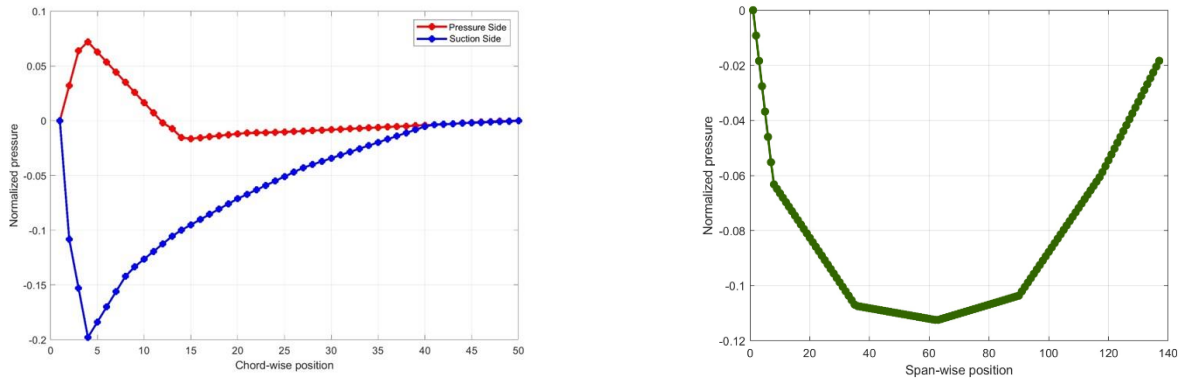

Figure 11: Chord-wise (left) and span-wise (right) pressure shapes.

Among the physical sensors used for response acquisition during tests, a subset of observations was chosen to evaluate the estimator performance. The remaining sensors were retained as reference quantities, serving to validate the accuracy of the estimated responses. From the total of 23 strain sensors depicted in Figure 12, only 13 strain (along Z direction) have been selected as measurements for the AKF: S3,S4,S5,S7,S8,S10,S11, S14,S17,S18,S19,S20,S21.

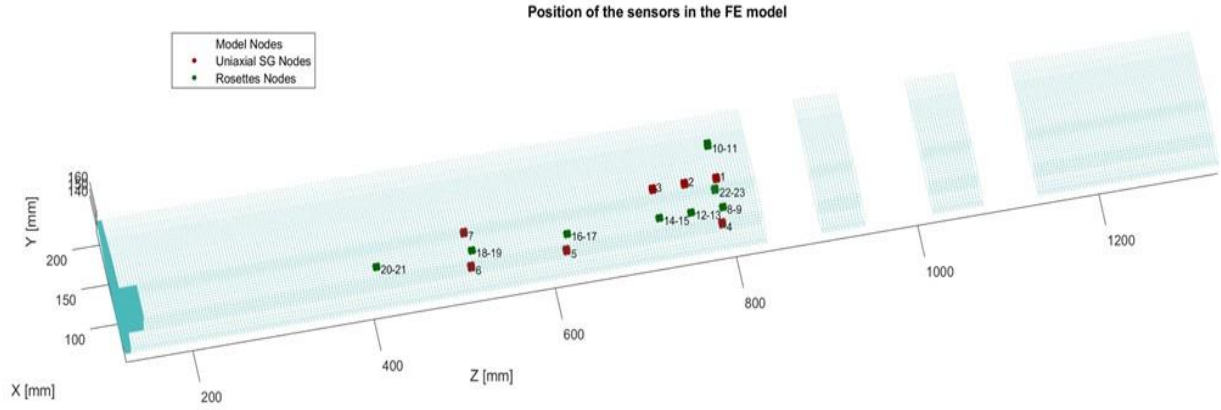

Figure 12: Sensors layout.

Given the system resting conditions at the start of the physical sensors recording, null values have been assigned to both $\mathbf{x}_0^{a-}$ and $\mathbf{P}_0^{a-}$ to initialize the AKF. The values populating the diagonal elements of the measurement noise covariance matrix $\mathbf{R}$ have been retrieved from background noise measurements operated during the test campaign. To the contrary, the diagonal values of the process noise covariance matrix $\mathbf{Q}^a$ have been set to 10^{-9} via a tuning process aimed at optimizing the filter accuracy.

Figure 13 reports on the strain response estimation for sensors S11, S12, S13. The included plots show a comparison of the time histories and autopowers of the estimated signals against the responses recorded at the same locations by the physical sensors. These plots confirm that the AKF allows precise strain response estimation at measured (S11) as well as unmeasured (S12, S13) locations. The same conclusion can be drawn by evaluating the estimation accuracy over the entire set of responses as reported in Figure 14, which shows the percentage 1-NRMSE (Normalized Root Mean Square Error) between each measured and estimated signal.

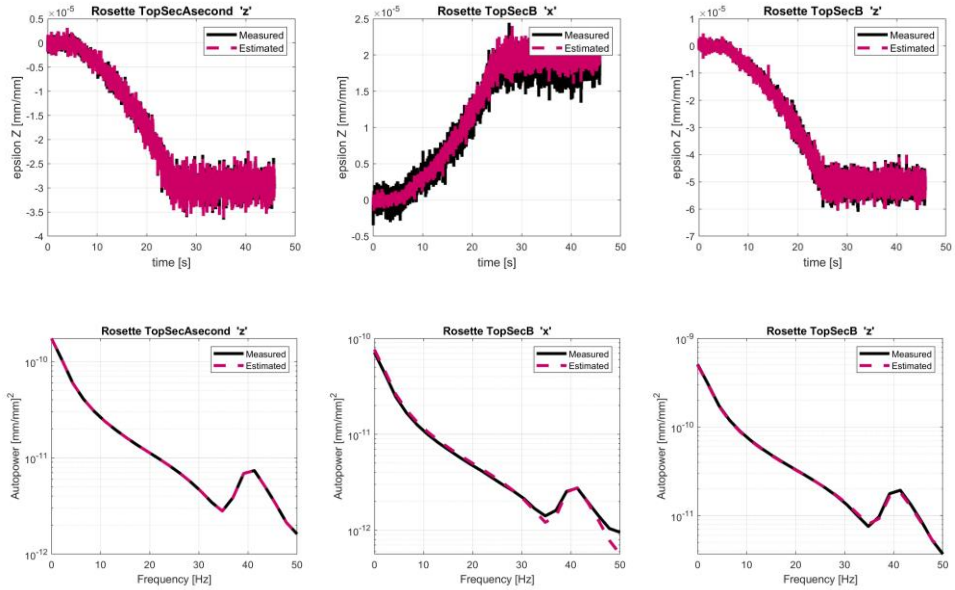

Figure 13: Time histories (top) and autopowers (bottom) of measured (black) and estimated (magenta) strain responses at S11 (left), S12 (center) and S13 (right).

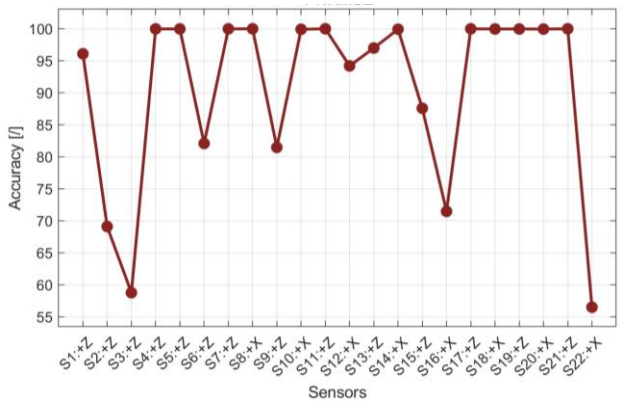

Figure 14: 1-NRMSE percentage indicator evolution over the entire set of strain responses.

The AKF input estimation performance can be evaluated by comparing the equivalent forces measured by the pressure ports and their corresponding estimates. The first can be computed via computation of the product between each pressure port reading and the area covered by such sensor on the wing surface. The AKF estimation instead, corresponds to the mapping at the pressure port location of the predicted master loads via the pressure shape matrix Ψ. Figure 15 shows this comparison in the time domain for pressure ports 1, 4, and 15. The locations of these pressure ports are visible in Figure 3. Figure 16 provides global information about this comparison by providing the accuracy indicator for the entire set of pressure ports distributed over the wing. Figure 15 and Figure 16 highlight that the employed approach allows for accurate identification of the unknown loading conditions, with an accuracy drop below 60% for only four pressure ports.

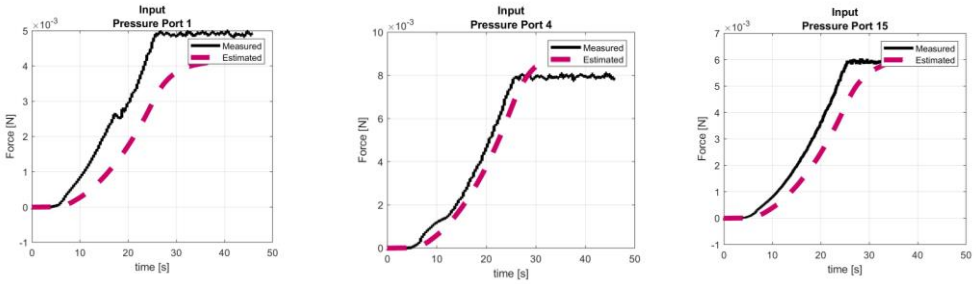

Figure 15: Time histories of measured (black) and estimated (magenta) forces at a pressure ports 1 (left), 4 (center), 15 (right).

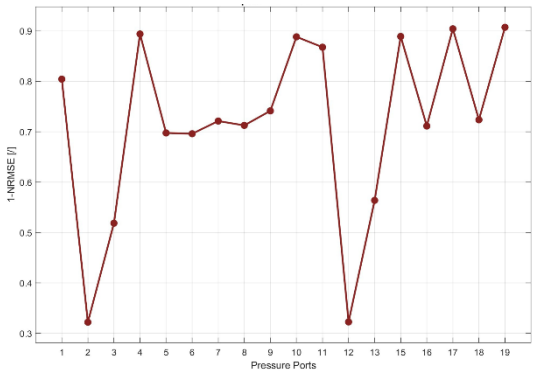

Figure 16: 1-NRMSE indicator evolution over the entire set of pressure ports.

3.3.3 Full-field structural response validation

This Section validated the full-field displacement estimation achieved via the AKF against the full-field displacement reconstructed via DIC. Figure 17 shows the time history and the autopower of the measured and the estimated displacements at three strategically selected nodes. The reported plots highlight that the estimated displacements over time are smaller than those measured by the DIC. This is also confirmed by Figure 18, which shows the full-field estimated and measured displacement at a fixed time instant. The limited displacement amplitudes obtained from the filter can be attributed to i) the observations provided to the filter solely capturing strain, providing no direct information about displacement; ii) the assumption of ideal clamping conditions in the FE model adopted for VS. This assumption also clarifies the lack of low-frequency modes (around 20-30 Hz) in the autopower graphs of the estimated displacements. Indeed, these low-frequency modes, which appear in the DIC autopower graphs, represent rigid body modes that the AKF estimation does not feature due to the ideal clamping assumption. Figure 19 reports on the accuracy of displacement estimation over the entire wing surface by reporting a contour plot of the 1-NRMSE indicator. This plot highlights that the overall displacement estimation accuracy ranges between 60 and 70 %.

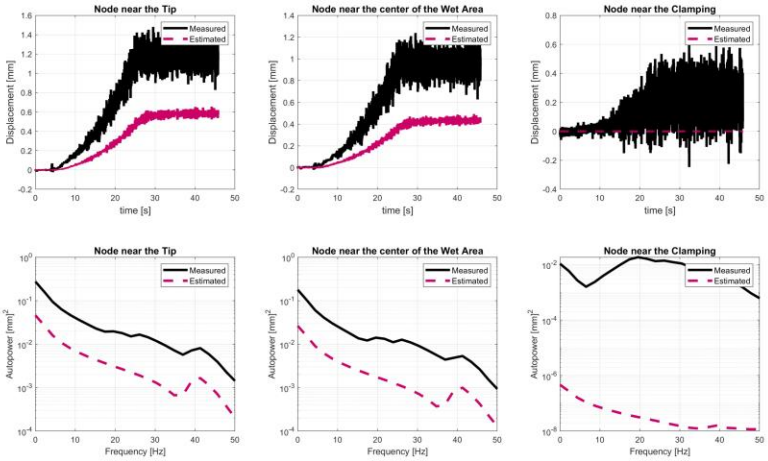

Figure 17: Time histories (top) and autopowers (bottom) of measured (black) and estimated (magenta) displacements at tip (left), mid wet area (center), clamping (right).

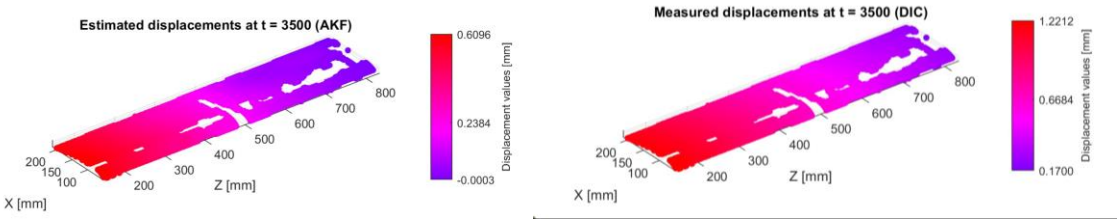

Figure 18: Estimated full-field displacement at fixed time instant: AKF (left) and DIC (right).

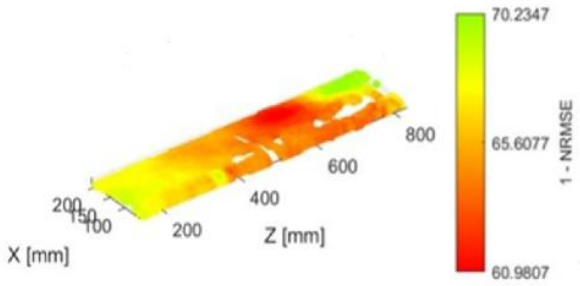

Figure 19: Full-field displacement 1-NRMSE indicator.

3.4 Computational Fluid Dynamics (CFD) analysis

The CFD model was created using Simcenter STAR-CCM+. The computational domain is bullet-shaped with a diameter *D* of 6000 mm.

The computational domain and the boundary conditions are represented in Figure 20.

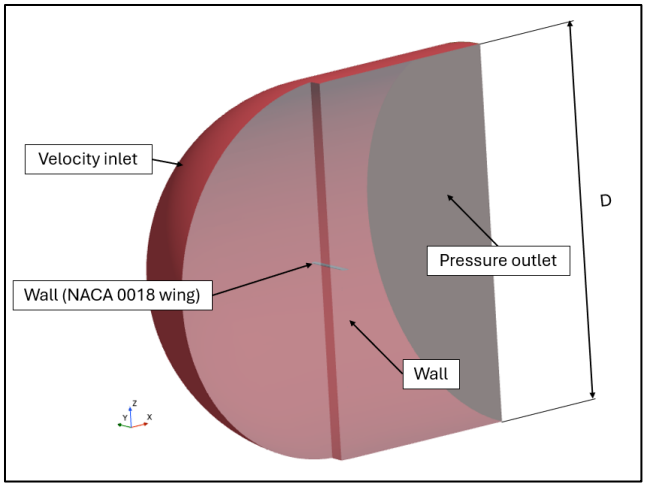

Figure 20: Computational domain with boundary conditions.

The main physics models implemented in the simulation are listed in **Error! Reference source not found.**.

Physics models	
Discretization method	Finite volume method
Solver	Implicit Unsteady
Approach	Segregated Fluid Isothermal
Turbulence Model	Shear Stress Transport k- ω
Temporal Discretization	1st order
Iteration for Time Step	5
Wall treatment	All y+ Wall Treatment

Table 3: Main physics models of the CFD simulation

The velocity magnitude at the inlet is defined along the x-direction, with a ramp that increases from 0 to 50 m/s over 25 seconds and then maintains this velocity for the remainder of the simulation.

The control volume has meshed with a polyhedral mesher. The transition between the far field and the surface of the wing has been realized with the prism layer mesher. The first layer of prism layers has a dimension of 0.004 mm, then cells grow in 16 layers up to the core mesh. The core mesh has a base dimension of 150 mm and a minimum size of 3 mm near the wing and in its wake (Figure *21*).

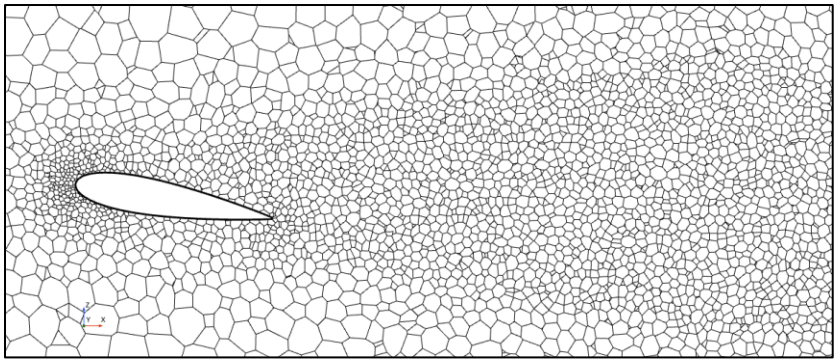

Figure 21: Mesh on section plane.

Pressure values were extracted from virtual probes placed on the wing at the same positions as the real sensors. The comparison between the CFD model and the experimental test was made on the suction side ports. **Error! Reference source not found.** shows the percentage difference between the numerical and experimental values.

Difference between CFD and experimental results (suction side) [%]											
PP1	**PP2**	**PP3**	**PP4**	**PP5**	**PP6**	**PP7**	**PP8**	**PP9**	**PP10**	**PP11**	**PP12**
8.55	-8.35	-6.36	7.23	5.10	-0.84	6.33	2.99	2.81	-2.13	-28.03	-5.67

Table 4: Comparison between CFD and experimental test.

An analysis of the pressure profiles on a section of the suction side along the span was also carried out. The chosen section is the one with the most pressure ports installed, specifically ports 5 to 12. Figure 22 shows that the CFD profile matches the experimental profile, demonstrating, along with the comparison shown in Table 4**Error! Reference source not found.**, that the CFD model is well-correlated.

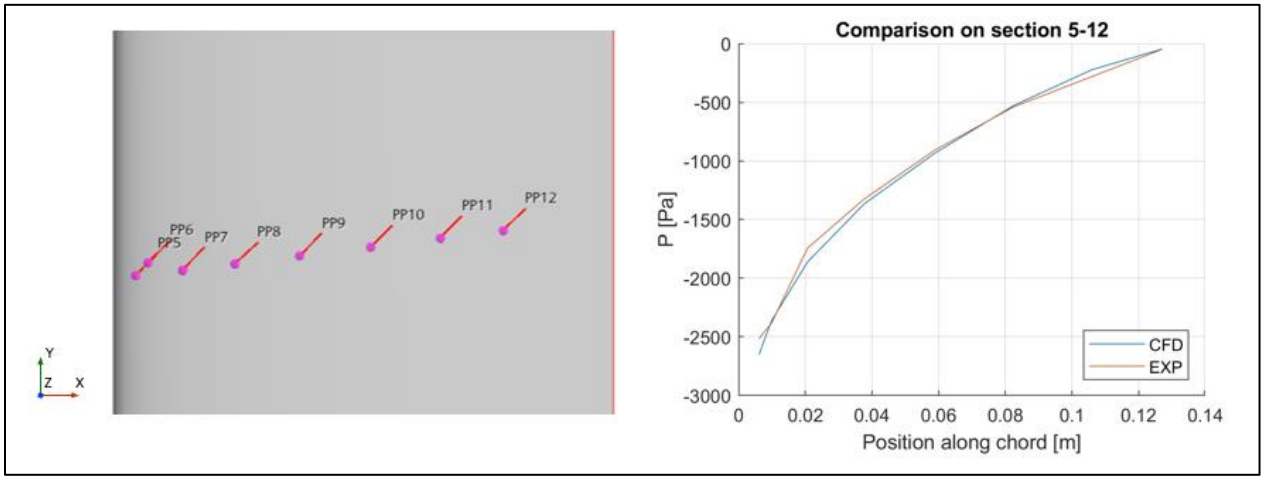

Figure 22: Comparison of pressure profiles on the PP 5-12 section.

Scalar scenes were also extracted to show velocity and pressure on the PP 5-12 section, providing a better visualization of the flow field behaviour, Figure 23.

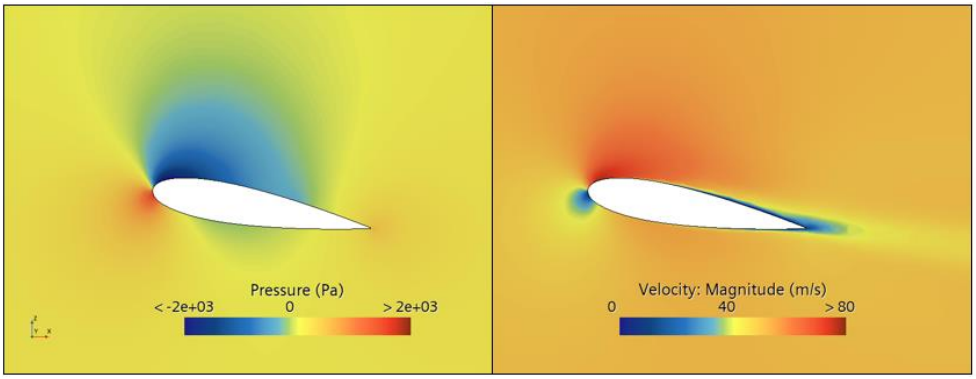

Figure 23. scalar scenes on the PP 5-12 section.

4 CONCLUSIONS AND NEXT STEPS

The main goal of this paper consisted in presenting an FSI analysis framework based on experimental (DIC), numerical (FEM and CFD), and hybrid approaches (VS), with specific focus on wind tunnel testing of an aluminum wing.

The test setup, the FE Model and its validation through experimental means, as well as the DIC and FE Model geometries alignment, were discussed. The implementation of the AKF for distributed loading conditions has been proposed and the achieved results have been compared to experimental data, including full-field displacement obtained via DIC. The latter comparison showed good accuracy (approximately 65%). It is worth noting that displacement estimation via AKF is particularly challenging due to the absence of displacement observations in the filter. Nonetheless, the validation against experimental strain sensor data yielded excellent results, underscoring the robustness of the approach. The pressure distribution over the wing surface has been also reconstructed via the enhanced AKF approach, providing good correlation with the pressure values measured by the pressure ports.

Future developments include improvement of the BCs during wind tunnel testing and its representation within the FEM. Additionally, a more flexible structure could be tested in order to increase the interaction between the fluid and the structure, thus allowing for more informative structural measurements via both strain gauges and DIC. The latter could be performed using a painted speckle to reduce noise and uncertainties in the DIC strain measurements. Additionally, the pressure distribution simulated via CFD will be used to retrieve the pressure shape matrix to be employed within the AKF. Finally, a numerical FSI analysis will be established to finalize the numerical activities complementing the experimental measurements.

ACKNOWLEDGMENTS

The authors acknowledge Flanders Make and the Hermes Fund for its support through the Project “VSFlex - Virtual Sensing on Flexible systems using distributed parameter models”, Project No. HBC.2019.0082.

The authors gratefully acknowledge Flanders Innovation & Entrepreneurship for its support of the Baekeland project ”Digital Image Correlation For Structural Dynamics Full-field Analysis”, Project No. HBC.2019.2595.

REFERENCES

[1] D. J. Anderson, Fundamentals of Aerodynamics. 6th ed., Columbus: McGraw-Hill Education, 2016.

[2] S. R. Singiresu, Mechanical Vibrations, Miami: Pearson Education, 2017.

[3] D. N. B. C. K. S. B. K. B. P. Fedorov V.A., "Investigation of Structural Behavior due to Bend-Twist Couplings in Wind Turbine Blades," in *ICCM*, 2009.

[4] A. S. N. a. J. V. Maheri, "Combined Analytical/FEA- Based Coupled Aero Structure Simulation of a Wind Turbine With Bend-Twist Adaptive Blades," *Renewable Energy,* vol. 32, pp. 916-930, 2007.

[5] P. Zhang, S. Peterson and M. Porfiri, Combined particle image velocimetry/digital image correlation for load estimation, Experimental Thermal and Fluid Science, 2019.

[6] G. Jacobi and A. Nila, Simultaneous PIV and DIC Measurements in a Towing Tank Environment with a Flexible Hydrofoil, 14th International Symposium on Particle Image Velocimetry, 2021.

[7] S. Vettori, E. Di Lorenzo, B. Peeters, M. M. Luczak and E. Chatzi, "An adaptive-noise Augmented Kalman Filter approach for input-state estimation in structural dynamics," *Mechanical Systems and Signal Processing,* vol. 184, 2023.

[8] E. Lourens, E. Reynders, G. de Roeck, G. Degrande and G. Lombaert, "An augmented Kalman filter for force identification in structural dynamics," *Mechanical Systems and Signal Processing,* vol. 27, pp. 446-460, 2012.

COPYRIGHT STATEMENT